

Cell-geometry-dependent changes in plasma membrane order direct stem cell signalling and fate

Thomas C. von Erlach^{1,2,3}, Sergio Bertazzo^{1,4}, Michele A. Wozniak⁵, Christine-Maria Horejs^{1,2,3}, Stephanie A. Maynard^{1,2,3}, Simon Attwood², Benjamin K. Robinson², Hélène Autefage^{1,2,3}, Charalambos Kallepitis^{1,2,3}, Armando del Río Hernández¹, Christopher S. Chen^{5,6,7}, Silvia Goldoni^{1,2,3*} and Molly M. Stevens^{1,2,3*}

Cell size and shape affect cellular processes such as cell survival, growth and differentiation^{1–4}, thus establishing cell geometry as a fundamental regulator of cell physiology. The contributions of the cytoskeleton, specifically actomyosin tension, to these effects have been described, but the exact biophysical mechanisms that translate changes in cell geometry to changes in cell behaviour remain mostly unresolved. Using a variety of innovative materials techniques, we demonstrate that the nanostructure and lipid assembly within the cell plasma membrane are regulated by cell geometry in a ligand-independent manner. These biophysical changes trigger signalling events involving the serine/threonine kinase Akt/protein kinase B (PKB) that direct cell-geometry-dependent mesenchymal stem cell differentiation. Our study defines a central regulatory role by plasma membrane ordered lipid raft microdomains in modulating stem cell differentiation with potential translational applications.

Proteomics and Förster resonance energy transfer (FRET) imaging studies suggest that cytoskeletal proteins interact and associate with plasma membrane lipid raft microdomains⁵, which are important regulators of cell signalling⁶. Using model membranes, it was proposed that the formation of actin cytoskeleton networks induces membrane phase separation and heterogeneity, indicating lipid raft formation⁷. Thus, events resulting in enhanced formation of cytoskeletal networks, such as integrin engagement with the extracellular matrix and focal adhesion formation were found to increase membrane order⁸, a biophysical hallmark of lipid rafts^{9,10}. We hypothesized that cell-architecture-related changes in cytoskeletal networks modulate lipid rafts independently of soluble extracellular cues. As a result, the biophysical state of the cytoskeleton directly regulates the activity of cell signalling proteins associated with plasma membrane microdomains. Although this has been shown in differentiated cell types, the relationship between rafts and cytoskeleton in mesenchymal stem cell function and fate is largely unknown. We cultured human mesenchymal stem cells (hMSCs) on surfaces micropatterned with fibronectin islands of triangular, square and circular geometries with identical surface area (1,350 μm^2). Cells adhered to fibronectin and displayed distinct

morphologies and cytoskeletal arrangement dictated by island geometries (Fig. 1a,b). Fluorescence intensity heat maps of F-actin and myosin IIa highlighted differences in cell contractility among the three geometries (Fig. 1c). Analysis of the compliance of living cells by atomic force microscopy (AFM) revealed differences in shape-dependent stiffness between triangular and circular, and square and circular cells. Higher stiffness measured in triangular and square cells correlated with cell contractility (Fig. 1d). The AFM data reveal a link between cell shape and elasticity, independently of adhesion area. To observe 3D structural arrangements of the plasma membrane, we serially sectioned cells in situ using focused ion beam (FIB) coupled to imaging (Fig. 2a). 3D reconstructions of plasma membranes brought to light remarkably different topographies across cell geometries down to the nanoscale (Fig. 2b). This observation correlated with a significantly increased number of membrane invaginations in the size range of 50–100 nm, resembling caveolae, a subset of lipid rafts, in triangular compared with circular cells (Fig. 2c,d, non-treated). These data point to a connection between cell contractility and caveolae formation. Interestingly, it was previously reported that white blood cells and neurons lack caveolae despite having planar-shaped lipid rafts¹¹. This suggests that caveolae are a product of surface area demand and supports the notion that cells with lower cytoskeletal contractility assemble less caveolae. Thus micropatterning cells in different shapes but with the same adhesion area can decouple area and cytoskeletal contractility. Next, we analysed the number of caveolae in triangular, square and circular hMSCs in the presence of cytochalasin D, a mycotoxin that interferes with actin polymerization. The treatment abolished cell-shape-dependent differences in caveolae abundance (Fig. 2d, CytoD). Furthermore, treatment with Y27632, a ROCK (Rho-associated kinase) inhibitor that blocks myosin IIa light chain phosphorylation and consequently actomyosin contraction, had a similar effect (Fig. 2d). As caveolae are cholesterol-rich structures, we tested methyl- β -cyclodextrin (M β CD), a cholesterol-sequestering agent that disrupts the integrity of lipid rafts¹². Treating hMSCs with M β CD lowered the number of caveolae across cell shapes compared with non-treated cells and erased geometry-dependent differences (Fig. 2d and Supplementary Fig. 1). Interestingly, treatment

¹Department of Materials, Imperial College London, London, UK. ²Department of Bioengineering, Imperial College London, London, UK. ³Institute of Biomedical Engineering, Imperial College London, London, UK. ⁴Department of Medical Physics & Biomedical Engineering, University College London, London, UK. ⁵Department of Bioengineering, University of Pennsylvania, Philadelphia, PA, USA. ⁶Department of Bioengineering and the Biological Design Center, Boston University, Boston, MA, USA. ⁷The Wyss Institute for Biologically Inspired Engineering, Harvard University, Boston, MA, USA.

*e-mail: s.goldoni22@gmail.com; m.stevens@imperial.ac.uk

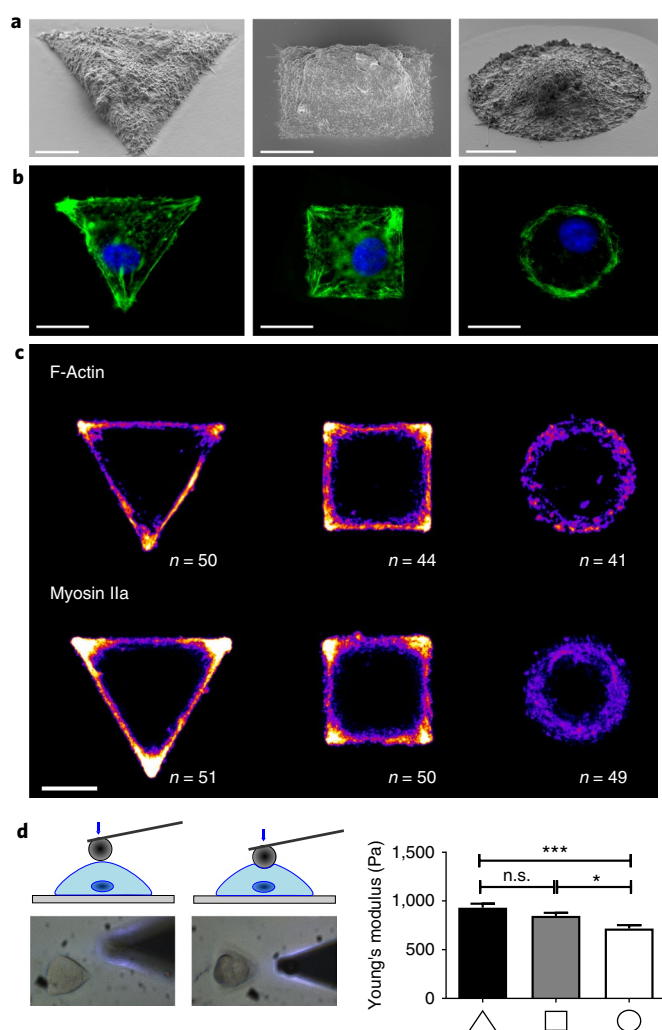


Fig. 1 | Cell geometry induces changes in cytoskeletal arrangement and cell contractility. **a**, Representative SEM micrographs of micropatterned hMSCs. Scale bars, 10 μ m. **b**, Representative immunofluorescence images of hMSCs stained for F-actin (green) and DAPI (blue). Scale bars, 20 μ m. **c**, Immunofluorescence intensity heat maps of myosin IIa and F-actin. Higher intensity is represented by a yellow/white colour. n = number of cells used for heat map generation. Scale bar, 20 μ m. **d**, Live cell stiffness measurement of triangular, square and circular cells by atomic force microscopy. Thirty cells per condition were analysed. *, $p < 0.05$; ***, $p < 0.001$; n.s., not significant. Error bars represent standard error of the mean (s.e.m.).

with M β CD did not impair cell spreading on fibronectin islands (Supplementary Fig. 2). However, F-actin staining revealed less actin bundling and focal organization in square and triangular cells supporting the interdependence between actin cytoskeleton and lipid rafts. This interdependence has been shown in neurons where cholesterol depletion results in aberrant axonal growth and guidance¹³.

We further investigated the relationship between geometrical cues and lipid rafts with total internal reflection fluorescence (TIRF) microscopy. We used fluorescein isothiocyanate (FITC)-conjugated cholera toxin B subunit (CTB), a GM1 gangliosides binder, and fluorescent filipin III. CTB binds specifically to lipid rafts¹⁴ and filipin III binds cholesterol¹⁵. We detected a higher FITC-CTB signal on the plasma membrane of triangular and square hMSCs compared with circular cells (2 and 1.5 fold, respectively). The intensity of

fluorescent filipin III was around 20% and 10% higher in triangular and square cells, respectively, compared with circular cells (Fig. 3a,b). The chemical heterogeneity of the plasma membrane across cell geometries correlates with the structural heterogeneity observed by FIB while the underlying biophysical mechanism and structure–function relationship are yet to be understood. Plasma membrane invaginations detected by FIB are likely caveolae based on their size and sensitivity to M β CD treatment. Because caveolae, a subtype of lipid rafts¹⁶, are caveolin-1 positive structures, we measured caveolin-1 expression on the plasma membrane of patterned hMSCs. TIRF imaging revealed around 20% more caveolin-1 expressed on the plasma membrane of triangular and square cells compared with circular cells (Fig. 3a,b) in line with the quantification of caveolae-like invaginations observed by FIB (Fig. 2a–d). The average distance of cells from the substrate was comparable across shapes, reducing the likelihood of differences detected by TIRF being artefactual (Supplementary Fig. 3). These data indicate that cell geometry regulates the abundance of lipid rafts and caveolae. In fact, CD71, a transferrin receptor associated to non-raft membrane domains, was equally expressed on the membrane of triangular and circular cells (Fig. 3c,d). To further probe the link between cytoskeletal contractility and caveolae, we imaged CTB and caveolin-1 in the presence or absence of Y27632. Disrupting the RhoA pathway abolished cell-shape-dependent differences in caveolae and lipid raft abundance (Fig. 3e,f), indicating that cytoskeletal contractility can regulate plasma membrane biophysics in an extracellular signalling-independent fashion. As expected, sequestering cholesterol with M β CD also erased cell-shape-dependent modulation of lipid rafts. It appears that M β CD treatment causes redistribution of Cav-1 from the periphery into internal regions within the substrate-facing plasma membrane in circular hMSCs, suggesting that cells are subjected to cytoskeletal rearrangement on M β CD treatment (Supplementary Fig. 4). Furthermore, the effect of cell shape on plasma membrane order was investigated by analysing giant plasma membrane vesicles (GPMVs) isolated from triangular, square and circular micropatterns using C-laurdan as reported elsewhere¹⁷. GPMVs from triangular cells displayed the highest membrane order (Fig. 3g,h), further suggesting that lipid rafts are more abundant in these cells. As a control, we analysed GPMVs from hMSCs grown in a tissue culture flask with or without M β CD (Supplementary Fig. 5).

Considering the cell signalling and endocytosis function of lipid rafts and caveolae¹⁶, we investigated whether the observed cell-geometry-dependent changes could trigger downstream signalling driving cell behaviour. It was recently reported that activity of the serine/threonine kinase Akt is regulated by its association with lipid rafts¹⁸. Lipid rafts facilitate recruitment to the inner leaflet of the plasma membrane and subsequent activation of Akt and its activator phosphoinositide-dependent kinase-1 (PDK1)^{19,20}. Furthermore, M β CD-mediated cholesterol depletion abolishes Akt signalling in keratinocytes²¹. Activated by growth factors, cytokines and ligand-independent stimuli, Akt and PDK1 are recruited to the plasma membrane resulting in the phosphorylation of Akt at T308 initiating a signal transduction cascade²². We measured Akt phosphorylation at the T308 site via the in-cell western (ICW) assay (Fig. 4a). In line with the differential lipid raft assembly in cells displaying high cytoskeletal contractility, we found significantly higher Akt T308 phosphorylation in triangular and square cells compared with circular cells (Fig. 4f, control). Since Akt recruitment to the plasma membrane is important for its activation, we quantified Akt abundance by TIRF microscopy (Fig. 4b). We found more Akt protein on the surface of triangular and square cells compared with circular cells (Fig. 4c). To explore Akt association to lipid rafts, we analysed the correlation of Akt and CTB signals in TIRF microscopy using Pearson's coefficient. Due to the resolution limit of TIRF microscopy, the co-localization is limited to plasma membrane microdomains. We found increased co-localization of CTB and Akt as well

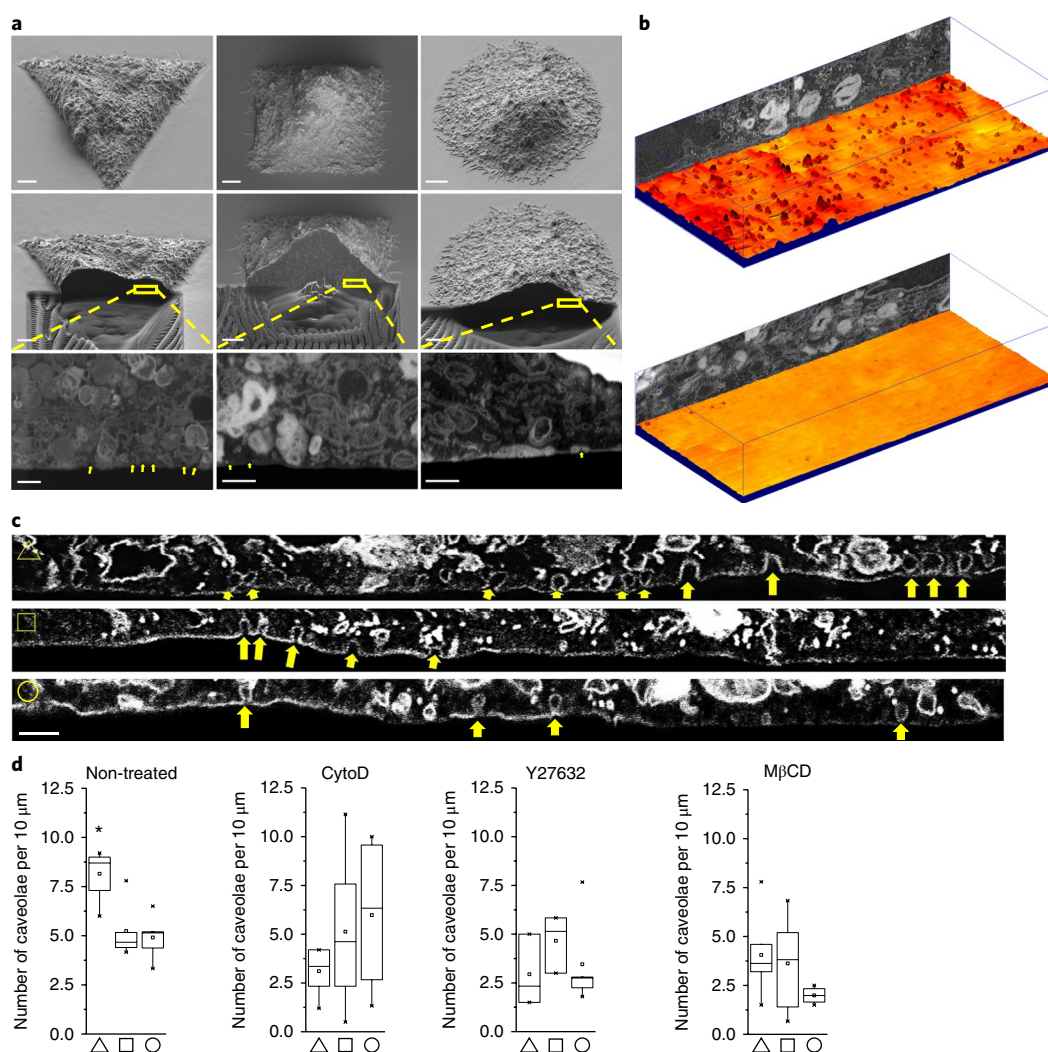


Fig. 2 | Cell geometry regulates plasma membrane morphology and topography. **a**, High-resolution electron micrographs of cells in situ generated by focused ion beam microscopy. Top row: SEM micrographs of triangular, square and circular micropatterned cells; middle row: micropatterned cells sectioned in the middle by focused ion beam; bottom row: cross-section analysed with high magnification reveals cell-geometry-dependent morphology of plasma membrane facing the substrate. Scale bars, 5 μm (top and middle); 0.5 μm (bottom). **b**, Cross-section and 3D reconstruction of plasma membrane surface illustrated as topographical heat map based on 60 cross-sections of triangular (top) and circular (bottom) cells. **c**, High-magnification micrographs focusing on the plasma membrane/substrate interface reveal the presence of membrane invaginations in the range of 50–100 nm resembling caveolae (yellow arrows). Scale bar, 300 nm. **d**, Number of caveolae-like structures quantified from images as in **c** of control hMSCs and cells treated as indicated. Data are obtained from 19 to 35 cross-section images from 3 to 6 cells per shape. *, $p < 0.05$. Data are presented as box plots to show values distribution; bottom and top of box represent 25% and 75%, respectively.

as Akt and PDK1 as compared with CAV-1–Akt, cellular Src kinase (c-Src)–Akt, CD71–CAV-1 and CD71–CTB, supporting the existence of an interaction between Akt and PDK1 in lipid rafts (Fig. 4d). To corroborate the ICW data and validate signal specificity, we ran a western blot for pan Akt and phospho-Akt T308 using the same antibodies used in the ICW assay (Fig. 4e). Western blots showed a decrease in Akt T308 phosphorylation in circular cells compared with triangular cells (non-cropped blots in Supplementary Fig. 6).

We further analysed the connection between cytoskeletal contractility, lipid rafts and Akt T308 phosphorylation using chemical inhibitors. Disrupting lipid rafts by M β CD or filipin III^{21,23} treatment reduced Akt T308 phosphorylation in high-contraction geometries abolishing shape-dependent differences (Fig. 4f). We observed a similar effect when treating with Y27632 and CytoD (Fig. 4f). The Akt allosteric inhibitor MK2206²⁴ also erased shape-driven Akt T308 phosphorylation (Supplementary Fig. 7). Importantly, MK2206 blocks the pleckstrin homology (PH) domain of Akt that

is required for lipid raft association. Taken together, these data demonstrate the existence of a previously unexplored mechanism of cell-geometry-dependent Akt activation mediated by cell contractility and lipid raft formation.

To further understand the molecular mechanism behind Akt activation by cell shape changes, we investigated the role of the Akt upstream activator phosphatidylinositol-3 kinase (PI3K). PI3K mediates conversion of membrane phosphatidylinositol 4,5-bisphosphate (PI(4,5)P₂) to phosphatidylinositol 3,4,5-trisphosphate (PI(3,4,5)P₃), which recruits both Akt and its activator PDK1 to the plasma membrane by direct interaction²⁵. We overexpressed a plasma-membrane-targeted, constitutively active PI3K in hMSCs. As expected, engineered cells displayed a higher level of Akt phosphorylation compared with control cells (Supplementary Fig. 7). Interestingly, hMSCs with increased PI3K activity did not display significant differences in shape-dependent Akt phosphorylation compared with control cells, indicating that the observed

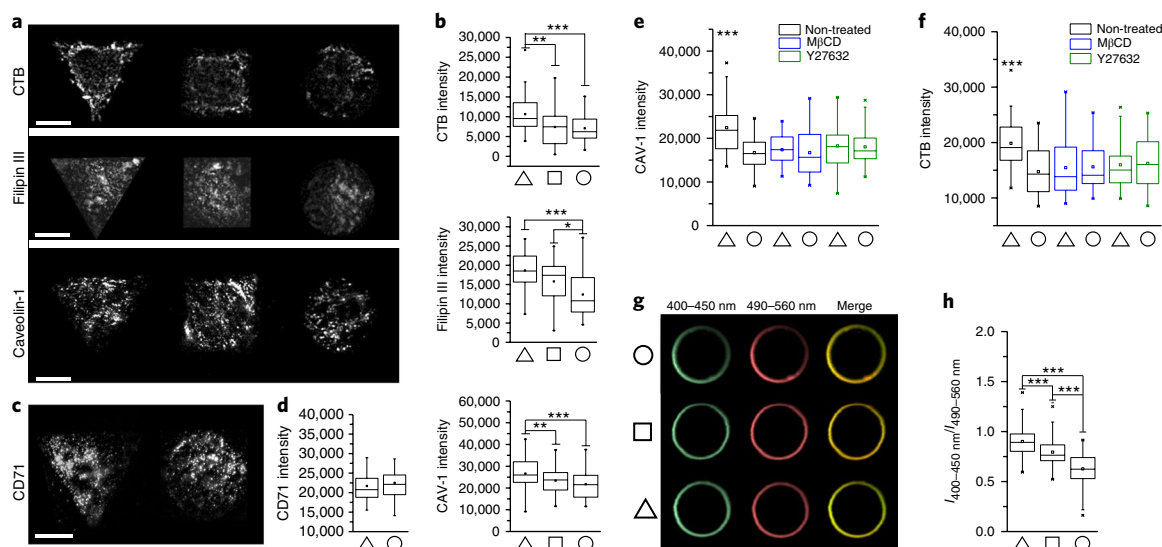


Fig. 3 | Signal intensity of lipid raft markers is dependent on cell geometry. **a**, Representative TIRF microscopy images of the plasma membrane/substrate interface. Cholera toxin subunit B (CTB) is a marker for lipid rafts and filipin III stains for accumulation of cholesterol, a hallmark of lipid rafts. Caveolin-1 positive plasma membrane domains are a subtype of lipid rafts. Scale bars, 20 μ m. **b**, Quantification of TIRF images per condition and stain ($n = 75$ –93 for CAV-1, $n = 33$ –37 for filipin III, $n = 38$ –53 for CTB). Box plots show complete data range, bottom and top of box represent 25% and 75%, respectively. ***, $p < 0.001$; **, $p < 0.01$; *, $p < 0.05$ (three independent experiments). **c**, Representative TIRF microscopy images of triangular and circular hMSCs stained for CD71, a non-raft marker. Scale bar, 20 μ m. **d**, Quantification of TIRF images of CD71 stained hMSCs (**c**) ($n = 20$ –32). **e**, **f**, Quantification of TIRF images of triangular and circular hMSCs (**a**), treated with either the ROCK inhibitor Y27632 or methyl- β -cyclodextrin (M β CD) ($n = 35$ –46 for CTB and $n = 29$ –42 for CAV-1). ***, $p < 0.001$. **g**, Representative multiphoton images of C-laurdan stained GPMVs isolated from triangular, square or circular hMSCs with emission light filtered to select wavelengths representative of ordered (green) and disordered (red) phase. **h**, Quantification of the ratio of fluorescence intensity, $I_{400-450 \text{ nm}}/I_{490-560 \text{ nm}}$, of the ordered (green) and disordered (red) phase emission of GPMVs isolated from triangular, square or circular hMSCs ($n = 51$ –123). Box plots show complete data range, bottom and top of box represent 25% and 75%, respectively. ***, $p < 0.001$ (three independent experiments).

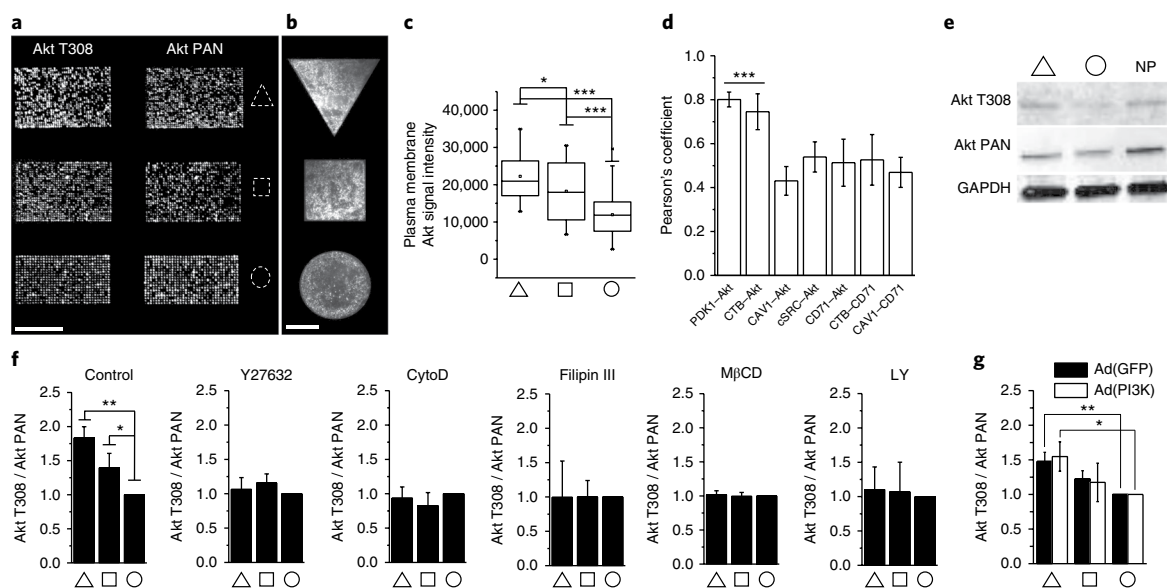


Fig. 4 | Akt recruitment to the plasma membrane and activation are dependent on cell geometry. **a**, Representative in-cell western images of arrays of micropatterned hMSCs (950 cells per shape). Cells were stained with phospho-Akt T308 and pan AKT antibodies. Scale bar, 1 mm. **b**, Representative TIRF images of Akt. Scale bar, 20 μ m. **c**, Quantification of TIRF images per shape (**b**), from three independent experiments. Box plots show complete data range, bottom and top of box represent 25% and 75%, respectively ($n = 34$ –46). ***, $p < 0.001$; *, $p < 0.05$. **d**, Co-localization analysis from TIRF images of markers indicated and Akt in triangular hMSCs quantified by the Pearson's coefficient ($n = 8$ –11). ***, $p < 0.001$. **e**, Representative western blot of phospho-Akt T308 and pan Akt of triangular and circular as well as non-patterned (NP) hMSCs. GAPDH was used as loading control. Note that antibodies used in the western blot are the same as those used in the in-cell western assay. **f**, Quantification of data from in-cell western images (**a**), of cells treated as indicated. CytoD, cytochalasin D; methyl- β -cyclodextrin (M β CD); LY, LY294002. Values are means \pm standard deviation (s.d.). *, $p < 0.05$; **, $p < 0.01$ (three independent experiments in duplicate). **g**, Quantification of phospho-Akt T308 and pan Akt by in-cell western images of hMSCs stably transfected to carry enhanced PI3K activity compared with GFP transfected control cells. Values are means \pm standard deviation (s.d.). *, $p < 0.05$; **, $p < 0.01$ (three independent experiments in duplicate).

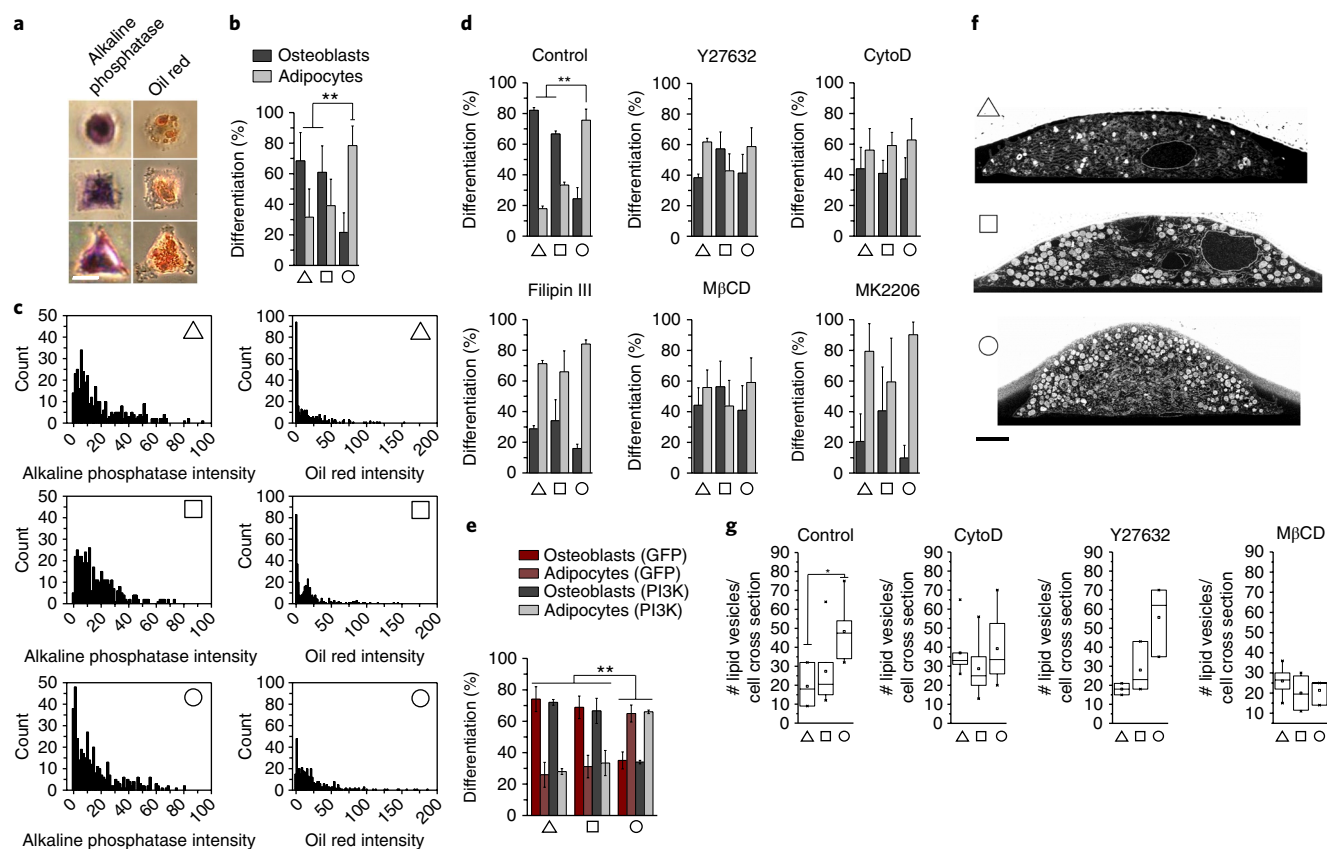


Fig. 5 | Lipid rafts and Akt signalling mediate cell-geometry-dependent hMSC differentiation. **a**, Representative images of hMSCs differentiated into either fat (OilRedO) or bone cells (alkaline phosphatase activity). Scale bar, 20 μ m. **b**, Quantification of differentiation of micropatterned hMSCs into either adipocytes or osteoblasts, following 7 days in the presence of a 1:1 mix of adipogenic and osteogenic differentiation medium. Compiled from cells from 7 independent experiments performed in duplicate ($n = 364$ – 392). Values are means \pm s.d. **, $p < 0.01$. **c**, Frequency histograms of OilRedO and alkaline phosphatase activity corresponding to data shown in **b**. **d**, Quantification of adipogenic and osteogenic fate (**a**) of micropatterned hMSCs treated as indicated. **e**, Quantification of adipogenic and osteogenic fate of hMSCs transfected with constitutively active PI3K. Values are means \pm s.d. **, $p < 0.01$. 100 cells per condition (three independent experiments in duplicate). **f**, Representative images of whole-cell cross-sections of triangular, square and circular hMSCs reveal the presence of characteristic lipid vacuoles (white round structures). Note the high density of lipid vacuoles in square and circular hMSCs, supporting evidence that low cell-contraction geometries favour adipogenesis. Cells are cultured in basal medium. Scale bar, 4 μ m. **g**, Quantification of lipid vacuoles from whole-cell cross-sections (**f**) of control hMSCs and cells treated as indicated. Data are obtained from 5 to 10 cells per shape. Data are presented as box plots to show values distribution; bottom and top of box represent 25% and 75%, respectively. *, $p < 0.05$.

mechanism is independent of the amount of phosphatidylinositol (3,4,5)-trisphosphate (PIP3) on the plasma membrane (Fig. 4g). On the contrary, inhibition of PI3K activity by LY294002, an inhibitor of the P110 catalytic subunit, abolished shape-dependent Akt T308 phosphorylation, indicating that PIP3 is required (Fig. 4f; LY; non-normalized data are shown in Supplementary Fig. 9). Additional protein kinases can be involved in this mechanism as LY294002 retains non-selective activity.

Lastly, we investigated the regulation of stem cell differentiation. Micropatterned hMSCs cultured in mixed adipogenic and osteogenic differentiation medium with low and high cytoskeletal contractility, differentiated preferentially into adipocytes and osteoblasts, respectively (Fig. 5a–c), as previously published^{2, 3, 26}. Differentiation was assessed in binary images with colour deconvolution of 7-day cultures stained with OilRedO and for alkaline phosphatase activity (Supplementary Fig. 10). Inhibition of cell contractility by Y27632 and CytoD led to the abolishment of cell shape differences since adipogenic differentiation increased by several fold in cell geometries with higher contractility (Fig. 5d). Remarkably, inhibiting lipid rafts with M β CD erased differences in lineage commitment dictated by cell shape and treating with filipin III resulted in an increase in adipogenesis in triangular and

square cells (Fig. 5d). These data bring to light the existence of a previously unknown mechanism that links lipid raft formation to hMSC differentiation. Importantly, treatment with MK2206 shifted overall differentiation towards adipogenesis without significant cell-geometry-dependent differences (Fig. 5d). These data define Akt as a major player in cell-geometry-dependent osteogenesis. We propose that high cell contractility favours lipid raft formation and/or stability, triggering Akt recruitment to the plasma membrane, pathway activation and osteogenic differentiation. In line with data presented in Fig. 4g, increased PI3K activity did not change cell-geometry-dependent differentiation (Fig. 5e). Interestingly, FIB cross-sections of whole hMSCs showed characteristic lipid vacuoles (Fig. 5f). Circular hMSCs carried a higher number of these structures, further supporting their preferential adipogenic phenotype (Fig. 5g). This phenotype is dependent on cytoskeletal contractility and the presence of lipid rafts as treatment with CytoD and M β CD reduced the shape-dependent differences (Fig. 5g).

To conclude, by applying innovative materials and imaging techniques, we investigated the cell/substrate interface and studied plasma membrane morphology at the nanoscale level. We discovered a mechanism by which cell geometry regulates cell signalling via modulation of plasma membrane order. Changes in plasma

membrane order due to geometric cues affect stem cell fate through a newly identified signalling mechanism involving Akt. Our data suggest a central role for lipid rafts in regulating cell behaviour and we propose that this mechanism allows cells to rapidly respond to changes in tissue mechanics and prepare for the integration of complex signals. Our findings expand the knowledge around tissue homeostasis mechanisms and have broad implications for regenerative medicine and tissue engineering applications^{27,28}.

Methods

Methods, including statements of data availability and any associated accession codes and references, are available at <https://doi.org/10.1038/s41563-017-0014-0>.

Received: 29 April 2014; Accepted: 18 December 2017;

Published online: 12 February 2018

References

- Chen, C. S., Mrksich, M., Huang, S., Whitesides, G. M. & Ingber, D. E. Geometric control of cell life and death. *Science* **276**, 1425–1428 (1997).
- Kilian, Ka, Bugarija, B., Lahn, B. T. & Mrksich, M. Geometric cues for directing the differentiation of mesenchymal stem cells. *Proc. Natl Acad. Sci. USA* **107**, 4872–4877 (2010).
- McBeath, R., Pirone, D. M., Nelson, C. M., Bhadriraju, K. & Chen, C. S. Cell shape, cytoskeletal tension, and RhoA regulate stem cell lineage commitment. *Dev. Cell* **6**, 483–495 (2004).
- Aragona, M. et al. A mechanical checkpoint controls multicellular growth through YAP/TAZ regulation by actin-processing factors. *Cell* **154**, 1047–1059 (2013).
- Head, B. P., Patel, H. H. & Insel, P. A. Interaction of membrane/lipid rafts with the cytoskeleton: impact on signaling and function: membrane/lipid rafts, mediators of cytoskeletal arrangement and cell signaling. *Biochim. Biophys. Acta* **1838**, 532–545 (2014).
- Simons, K. & Toomre, D. Lipid rafts and signal transduction. *Nat. Rev. Mol. Cell Biol.* **1**, 31–39 (2000).
- Liu, A. P. & Fletcher, D. A. Actin polymerization serves as a membrane domain switch in model lipid bilayers. *Biophys. J.* **91**, 4064–4070 (2006).
- Gaus, K., Le Lay, S., Balasubramanian, N. & Schwartz, M. Integrin-mediated adhesion regulates membrane order. *J. Cell Biol.* **174**, 725–734 (2006).
- Head, B. P. et al. Microtubules and actin microfilaments regulate lipid raft/caveolae localization of adenylyl cyclase signaling components. *J. Biol. Chem.* **281**, 26391–26399 (2006).
- Lingwood, D. & Simons, K. Lipid rafts as a membrane-organizing principle. *Science* **327**, 46–50 (2010).
- Head, B. P. & Insel, P. A. Do caveolins regulate cells by actions outside of caveolae? *Trends Cell Biol.* **17**, 51–57 (2007).
- Palazzo, A. F., Eng, C. H., Schlaepfer, D. D., Marcantonio, E. E. & Gundersen, G. G. Localized stabilization of microtubules by integrin- and FAK-facilitated Rho signaling. *Science* **303**, 836–839 (2004).
- Kamiguchi, H. The region-specific activities of lipid rafts during axon growth and guidance. *J. Neurochem.* **98**, 330–335 (2006).
- Blank, N. et al. Cholera toxin binds to lipid rafts but has a limited specificity for ganglioside GM1. *Immunol. Cell Biol.* **85**, 378–382 (2007).
- Wüstner, D. Fluorescent sterols as tools in membrane biophysics and cell biology. *Chem. Phys. Lipids* **146**, 1–25 (2007).
- Parton, R. G. & Simons, K. The multiple faces of caveolae. *Nat. Rev. Mol. Cell Biol.* **8**, 185–194 (2007).
- Sezgin, E. et al. Elucidating membrane structure and protein behavior using giant plasma membrane vesicles. *Nat. Protoc.* **7**, 1042–1051 (2012).
- Gao, X. & Zhang, J. Spatiotemporal analysis of differential Akt regulation in plasma membrane microdomains. *Mol. Biol. Cell* **19**, 4366–4373 (2008).
- Lasserre, R. et al. Raft nanodomains contribute to Akt/PKB plasma membrane recruitment and activation. *Nat. Chem. Biol.* **4**, 538–547 (2008).
- Gao, X. et al. PI3K/Akt signaling requires spatial compartmentalization in plasma membrane microdomains. *Proc. Natl Acad. Sci. USA* **108**, 14509–14514 (2011).
- Calay, D. et al. Inhibition of Akt signaling by exclusion from lipid rafts in normal and transformed epidermal keratinocytes. *J. Investigative Dermatol.* **130**, 1136–1145 (2010).
- Manning, B. D. & Cantley, L. C. AKT/PKB signaling: navigating downstream. *Cell* **129**, 1261–1274 (2007).
- Schnitzer, J. E., Oh, P., Pinney, E. & Allard, J. Filipin-sensitive caveolae-mediated transport in endothelium: reduced transcytosis, scavenger endocytosis, and capillary permeability of select macromolecules. *J. Cell Biol.* **127**, 1217–1232 (1994).
- Hirai, H. et al. MK-2206, an allosteric Akt inhibitor, enhances antitumor efficacy by standard chemotherapeutic agents or molecular targeted drugs in vitro and in vivo. *Mol. Cancer Therapeutics* **9**, 1956–1967 (2010).
- Vanhaesebroeck, B., Stephens, L. & Hawkins, P. PI3K signalling: the path to discovery and understanding. *Nat. Rev. Mol. Cell Biol.* **13**, 195–203 (2012).
- Müller, P., Langenbach, A., Kaminski, A. & Rychly, J. Modulating the actin cytoskeleton affects mechanically induced signal transduction and differentiation in mesenchymal stem cells. *PLoS ONE* **8**, 1–8 (2013).
- Stevens, M. M. & George, J. H. Exploring and engineering the cell surface interface. *Science* **310**, 1135–1138 (2005).
- Place, E. S., Evans, N. D. & Stevens, M. M. Complexity in biomaterials for tissue engineering. *Nat. Mater.* **8**, 457–470 (2009).

Acknowledgements

We thank H. M. Textor and F. Anderegg (ETH Zurich) for providing silicon masters for micro-contact printing as well as S. Rothery for training and guidance regarding TIRF microscopy (FILM facility at Imperial College London). T.C.v.E. was supported by an EPSRC DTA PhD award. S.B. was supported by the Rosetrees Trust and the Stonegate Trust and the Junior Research Fellowship scheme at Imperial College London. M.M.S. gratefully acknowledges ERC starting grant “NaturaLe” for funding (206807), Wellcome Trust Senior Investigator Award (098411/Z/12/Z) and the Rosetrees Trust. A.D.R.H. gratefully acknowledges ERC starting grant “ForceRegulation” (282051).

Author contributions

T.C.v.E. designed experiments, developed the substrates and conducted experiments, analysed and interpreted the data and wrote the manuscript. S.B. designed and carried out ion and electron microscopy experiments and analysed the data. M.A.W. conducted viral transfection experiments and revised the manuscript. C.K. performed 3D plasma membrane reconstruction and analysis. B.K.R. and S.A. conducted AFM measurements. C.-M.H. carried out western blots. C.S.C. revised the manuscript and consulted in experimental design. A.D.R.H. revised the manuscript and supervised S.A. H.A. helped with hMSC cultivation and differentiation experiments and revised the manuscript. S.A.M. helped with cell micropattern preparations and revised the manuscript. S.G. supervised the project, helped in experimental design, data analysis and interpretation, and co-wrote the manuscript. M.M.S. supervised the project, co-wrote the manuscript and helped in experimental design and data interpretation.

Competing interests

The authors declare no competing financial interests.

Additional information

Supplementary information is available for this paper at <https://doi.org/10.1038/s41563-017-0014-0>.

Reprints and permissions information is available at www.nature.com/reprints.

Correspondence and requests for materials should be addressed to S.G. or M.M.S.

Publisher's note: Springer Nature remains neutral with regard to jurisdictional claims in published maps and institutional affiliations.

Methods

Generation of micropatterned substrates. Micropatterned substrates were produced according to previously described protocols^{29,30}. Briefly, polydimethylsiloxane (PDMS, Sylgard 184; Dow Corning) stamps were generated by replica casting against a silicon master made by photolithography (gift from H. M. Textor). Immediately before microcontact printing, stamps were washed and treated with air plasma for 1 min (200 mtorr) (Plasma Prep 5, Gala Instruments). Then, the stamps were inked by immersion in bovine fibronectin (Sigma) solution (50 µg ml⁻¹ in phosphate-buffered saline (PBS)) for 1 h. Afterwards, blow dried stamps were placed in conformal contact with the substrate (non-treated polystyrene multi-dish, Nunclon Surface). The non-patterned area was then passivated by adding a Pluronic F127 (Sigma) solution (0.4% w/v in PBS) for 2 h. Micropatterns for TIRF were generated by using silanized glass as a substrate for cell micropattern preparation according to a protocol published previously³¹.

Culture of human mesenchymal stem cells and differentiation protocol. Human mesenchymal stem cells (hMSCs) (PromoCell) were cultured and seeded on micropatterned substrates according to a previously described protocol²⁹. Briefly, hMSCs were cultured in mesenchymal stem cell growth medium (PromoCell) using standard cultivation conditions (37 °C, 5% CO₂). For cell micropattern generation, cells were trypsinized (0.25% v/v trypsin-ethylenediaminetetraacetic acid (EDTA) solution (Invitrogen)) and seeded in serum-free growth medium at a density of 13,000 cells per cm². After 2 h incubation, cells were fully adhered and spread, and the samples were washed with PBS followed by the addition of serum-containing media. For differentiation, mesenchymal stem cell adipogenic and osteogenic differentiation medium was used (both from PromoCell).

Antibodies and reagents. Mouse monoclonal anti-phospho-Akt (T308) (1:200), anti-phospho-Akt (Ser 473), polyclonal rabbit anti-Akt (1:300), polyclonal rabbit anti-myosin IIa light chain (1:400), monoclonal rabbit anti-CD71, monoclonal rabbit anti-Src, monoclonal rabbit anti-PDK1 as well as monoclonal mouse anti-phospho myosin IIa light chain (1:100) were all purchased from Cell Signaling Technology. Glyceraldehyde 3-phosphate dehydrogenase (GAPDH) was bought from Ambion. FITC-conjugated cholera toxin B subunit (1:50) as well as filipin III from *Streptomyces filipinensis* (1:10) were purchased from Sigma. Alexa Fluor 488 and Alexa Fluor 568 phalloidin (1:300) and DAPI (4',6-diamidino-2-phenylindole) were all obtained from Molecular Probes (Invitrogen). Polyclonal rabbit anti-caveolin-1 (1:400) was purchased from Abcam. Secondary antibodies anti-mouse Alexa Fluor 568 (1:400) and anti-rabbit Fluor 488 (1:400) were bought from Molecular Probes. Infrared secondary antibodies, IRDye 680RD goat anti-mouse IgG and IRDye 800CW anti-rabbit (both 1:1,000) were purchased from LiCor. For inhibitor studies, the following concentrations were used: 2.5 µM Y27632, 40 nM cytochalasin D (both from Sigma), 3 µM MK2206 (Active Biochemicals), 0.5 mM methyl-β-cyclodextrin (Santa Cruz Biotechnology), 0.5 µM filipin III and 20 µM LY294002 (both from Cayman Chemicals). Concentrations were determined based on cell morphology analysis. Y27632 and methyl-β-cyclodextrin were both solubilized in PBS, all other inhibitors were solubilized in dimethyl sulfoxide (DMSO) according to manufacturer instructions.

AdPI3K transfection. hMSCs were maintained in growth media (10% v/v fetal bovine serum (FBS) in low-glucose Dulbecco's modified Eagle's medium (DMEM)). hMSCs were plated at a confluency of 13,000 cells per cm² overnight, and the next day infected with either GFP or PI3K-p110CAAX (AdPI3K) virus for 5 h. The following day, cells were trypsinized and 13,000 cells per cm² were plated on Pluronic-blocked micropatterned substrates in the presence of growth media or differentiation media for Akt activity assays or differentiation assays, respectively. Differentiation medium consisted of 1:1 adipogenic:osteogenic media and was changed every 3 days. Adipogenic media contained 3% v/v FBS, 1% v/v penicillin-streptomycin, 500 µM 3-Isobutyl-1-methylxanthine (IBMX), 2 µM rosiglitazone, 1 µM dexamethasone, 17 µM pantothene, 33 µM biotin and 1 µM insulin in DMEM/F12. Osteogenic media contained 10% v/v FBS, 1% v/v penicillin-streptomycin, 100 nM dexamethasone, 250 µM ascorbic acid-2-phosphate and 10 mM β-glycerophosphate.

Giant plasma membrane vesicle isolation and analysis. Giant plasma membrane vesicles (GPMVs) were isolated and analysed according to a previously published protocol¹⁷. Briefly, hMSCs were cultured on triangular, square and circular micropatterns for 24 h, washed with GPMV buffer (10 mM 4-(2-hydroxyethyl)-1-piperazineethanesulfonic acid (HEPES), 150 mM NaCl, 2 mM CaCl₂, pH 7.4) and then incubated in GPMV isolation solution (25 mM paraformaldehyde / 2 mM dithiothreitol in GPMV buffer) for 2 h. Afterwards, the solution was collected and transferred into bovine serum albumin (BSA)-coated vials. After 30 min, 50 µl from the bottom of the vial was transferred into a fresh BSA-coated vial and labelled with 1 µl of 0.2 mM solution of 6-dodecanoyl-2-dimethylaminonaphthalene (C-laurdan) (Molecular Probes) for 30 min.

Microscopy data analysis. For fluorescence analysis, cells grown on micropatterns were immunostained using standard procedures described previously³⁰. Briefly, formalin-fixed cell samples were permeabilized with 0.25% v/v Triton-X-100/

PBS for 2 min followed by blocking in bovine serum albumin solution (4% w/v in PBS). Primary and secondary antibodies staining was performed for 1 h in blocking buffer at room temperature. For TIRF microscopy analysis using plasma membrane lipid markers CTB and filipin III, samples were not permeabilized with Triton-X-100 to preserve the plasma membrane. Only single cells that were confined into the desired shape were selected by using the microscope in bright-field mode. An Olympus BX51 upright and an Olympus inverted microscope were used to image fluorescence and phase contrast samples. For the histological analysis, cells were inspected by phase contrast to determine whether they expressed lineage-specific markers based on what has been described previously². Briefly, for patterned hMSCs, only single cells that adhered to the pattern were used for statistical analysis. Cells that contained lipid vacuoles stained red by OilRedO were counted as adipocyte specification. Cells that stained blue for alkaline phosphatase were counted as osteoblast committed cells. For additional quantitation we performed a colour deconvolution of all cells across a surface stained with both markers based on what was published earlier². Briefly, raw RGB images acquired by phase contrast with a 20× objective were imported in ImageJ, background-subtracted and afterwards colour deconvoluted by a publicly available colour deconvolution plugin for ImageJ commonly used for separating similar histology stains (<http://www.dentistry.bham.ac.uk/landing/software/cdeconv/cdeconv.html>) with colour-specific vectors adapted to the particular images. The resulting separated red and blue channels were binarized with a set threshold based on visual examination and subsequently quantified. The generation of immunofluorescence heat maps was performed as described previously^{2,29}; briefly, fluorescent images of cell samples were obtained on the same day and using the same microscope and camera settings. Raw fluorescent images were background-subtracted in ImageJ, incorporated and aligned into a Z hyperstack and the summarized intensity was calculated for heat map generation. For total internal reflection fluorescence (TIRF) microscopy, samples on glass substrate (glass bottom dish, MatTek product number P35G-0-10-C) in PBS were imaged using a TIRF microscope as described previously^{30,32} using a 488 nm laser diode and a 100×/1.45 W Alpha Plan Fluor objective. Resulting 16 bit raw images were background-subtracted and binarized for quantification purposes using ImageJ software. For high-resolution co-localization analysis, background-subtracted TIRF microscopy images of two different channels were merged into one image. Then, Pearson's coefficient was analysed with ImageJ using the JACoP Plugin (<http://rsb.info.nih.gov/ij/plugins/track/jacop2.html>). Multiphoton imaging of C-laurdan-labelled GPMVs was performed with an inverted Olympus IX81 microscope with a 25× water immersion long working distance objective using a MaiTaiDeepSea Laser at 800 nm excitation and emission filtered at 410–440 nm as well as at 502–548 nm.

Western blot, in-cell western and immunofluorescence assays. For the in-cell western assay, cellular proteins were quantitated in situ based on infrared intensity. Samples were immunolabelled with an infrared conjugated IgG secondary antibody using standard immunofluorescence protocol and imaged using an Odyssey Fc Infrared Imaging System (LiCor) in the highest resolution (21 µm). The resulting signal intensity was subsequently quantified by using the Odyssey CLX Image Studio Analysis Software. Western blots were performed according to a standardized procedure published previously³³. Briefly, Ad(GFP) and Ad(PI3K) cells were lysed in 25 mM HEPES, 75 mM NaCl, 1% v/v tertigol-type nonyl phenoxypolyethoxylethanol (NP-40), 1 mM EDTA, 1× Halt protease and phosphatase inhibitor cocktail (Thermo Scientific), and centrifuged at 14,000 r.p.m. for 10 min at 4 °C. Lysates from cells were obtained with radioimmunoprecipitation assay (RIPA) buffer (Sigma) containing protease inhibitors (Roche) and phosphatase inhibitors (Sigma). Protein concentration was determined by Precision Red Advanced Protein Assay (Cytoskeleton). Ten micrograms of protein were separated by denaturing sodium dodecyl sulfate polyacrylamide gel electrophoresis (SDS-PAGE), transferred to a poly(vinylidene fluoride) (PVDF) membrane, blocked with 5% w/v BSA in 0.3% v/v Tween-20 in Tris-buffered saline, immunoblotted with primary antibodies (1:1,000), and detected using horseradish peroxidase-conjugated secondary antibodies (1:5,000; Jackson ImmunoResearch Laboratories) and SuperSignal West Dura (Pierce). Densitometric analysis was done by using a VersaDoc imaging system and QuantityOne software (Bio-Rad Laboratories). Western blot was performed using infrared labelled secondary antibodies, scanned and analysed using the Odyssey imaging system and software (LiCor).

Atomic force microscopy analysis. hMSCs were cultured on the three micropatterned shapes for 24 h. Samples were analysed in the Petri dish in PBS at room temperature by atomic force spectroscopy. A Nanowizard I (JPK, Germany) atomic force microscope (AFM) with an inverted microscope (IX-81, Olympus, Germany) was used for all measurements. We used MLCT-D levers (Bruker) with a nominal spring constant of 0.03 N m⁻¹. For analysis, cantilevers were calibrated immediately before use using the thermal noise method. Polystyrene microspheres with a diameter of 15 µm (Life Technologies) were attached to AFM cantilever tips using a UV curable glue (Loctite 350, rs-online) as described elsewhere³⁴. Force-displacement curves were analysed using a custom developed routine in Matlab (MathWorks). The contact point was identified by considering each point

in the approach curve and fitting the Hertz model to the contact region and a constant value for the points thereafter. The point with the smallest error for the combined fits was identified as the contact point. The Young modulus, E , was then determined for the contact region from this point onwards. Indentation was kept below 10% of the cell height to avoid substrate effects.

Focused ion beam and scanning electron microscopy analyses. Sample preparation was performed based on previously published methods³⁵. Sample fixation of micropatterned cells was performed at room temperature for 15 min using a 4% v/v formaldehyde (Sigma, BioReagent, $\geq 36.0\%$) with 0.2% v/v glutaraldehyde (Electron Microscopy Sciences) solution in PBS. After washing the samples three times with cacodilate buffer (Electron Microscopy Sciences), the samples were osmicated with osmium tetroxide in 2% w/v cacodilate buffer for 30 min. Then, samples were washed five times with deionized water and then dehydrated through a graded ethanol (Sigma, ACS reagent 99.5%) series. After dehydration, samples were infiltrated with Epon Resin (Electron Microscopy Sciences) by incubating the samples in a diluted series of ethanol-Epon Resin at a 3:1, 2:1 and 1:1 ratio for 1 h each, and then overnight at 1:2 ratio. After that, pure resin was added, changed twice in the first 12 h and then incubated again overnight. Then, the maximum amount of resin was removed and the bottom of the well plate (containing the cells) was detached and centrifuged at 5,000 r.p.m. for 5 min. Samples were immediately placed in an oven at 60 °C and left to cure overnight. Then, samples were placed on a SEM aluminium sample holder with carbon tape and silver paint was applied to the surrounding area of the sample to maximize conductivity. Afterwards, the samples were coated with a 5 nm chromium layer in a sputter coater (Quorum Technologies model K575X). Following the coating procedure, samples were introduced into an SEM/focused ion beam (Carl Zeiss, Auriga) with gallium ion beam operated at 30 kV. A region over the cells with approximately $15 \times 5 \times 2 \mu\text{m}$ (length \times height \times depth) was milled using 4 nA current. After that, the region exposed by the first milling was polished with 240 pA current and imaged by a backscattering detector with the electron beam operating at 1.5 V. To generate a 3D-surface model, individual high-resolution in situ cross-section electron micrographs of micropatterned cells were stacked using Matlab. From these volume datasets, an isosurface was extracted based on polygonal abstraction. The area between the substrate surface and substrate facing the cell plasma membrane was calculated by using the Image J software.

Statistical analysis. All data were analysed by one-way ANOVA followed by a Tukey and Bonferroni post hoc analysis except AFM data in Fig. 1d that was analysed by one-way ANOVA followed by a Bartlett's test for equal variances. The statistical parameters are as follows: Fig. 1d (F -value = 8.18, R square = 0.04415); Fig. 2d (F -value = 7.31 p -value triangular versus square cells = 0.027, p -value triangular versus circular cells = 0.014); Fig. 3b CAV-1 (F -value = 12.04, p -value triangular versus square cells = 0.0031, p -value triangular versus circular cells = 9.02261×10^{-6}); Fig. 3b CTB (F -value = 8.64, p -value triangular versus square cells = 0.00149, p -value triangular versus circular cells = 7.84×10^{-4}); Fig. 3b filipin III (F -value = 11.33, p -value circular versus square cells = 0.032, p -value triangular versus circular cells = 1.90×10^{-5}); Fig. 3e (F -value = 6.65, p -value non-treated triangular versus circular cells = 1.32×10^{-5} , p -value non-treated triangular versus triangular MBCD treated cells = 3.50×10^{-4} , p -value non-treated triangular versus circular MBCD treated cells = 2.07×10^{-5} , p -value non-treated triangular versus triangular Y27632 treated cells = 0.00356, p -value non-treated triangular versus circular Y27632 treated cells = 0.0019); Fig. 3f (F -value = 6.14, p -value non-treated triangular versus circular cells = 2.12×10^{-5} , p -value non-treated triangular versus triangular MBCD treated cells = 5.34×10^{-4} ,

p -value non-treated triangular versus circular MBCD treated cells = 9.24×10^{-4} , p -value non-treated triangular versus triangular Y27632 treated cells = 0.00143, p -value non-treated triangular versus circular Y27632 treated cells = 0.00594); Fig. 3h (F -value = 45.22, p -value triangular versus square cells = 2.22×10^{-5} , p -value triangular versus circular cells = 5.42×10^{-18} , p -value square versus circular cells = 3.58×10^{-9}); Fig. 4c (F -value = 26.42, p -value triangular versus square cells = 0.03, p -value triangular versus circular cells = 3.09×10^{-10} , p -value square versus circular cells = 1.02×10^{-4}); Fig. 4d (F -value = 29.91, p -values: Akt and CAV-1 versus CTB and CD71 = 0.23854, Akt and PDK1 versus CAV and CD71 = 3.99×10^{-12} , Akt and PDK1 versus CTB and CD71 = 5.33×10^{-9} , Akt and PDK1 versus Akt and CAV-1 = 1.38×10^{-13} , Akt and CTB versus CAV and CD71 = 2.21×10^{-9} , Akt and CTB versus CTB and CD71 = 2.42×10^{-6} , Akt and CTB versus Akt and CAV-1 = 6.17×10^{-11} , Akt and Cd71 versus Akt and CAV-1 = 0.46, Akt and Cd71 versus Akt and PDK1 = 3.01×10^{-10} , Akt and Cd71 versus Akt and CTB = 1.91×10^{-7} , Akt and c-Src versus Akt and CAV-1 = 0.11, Akt and c-Src versus Akt and PDK1 = 4.95×10^{-8} , Akt and c-Src versus Akt and CTB = 1.75×10^{-5}); Fig. 4f (F -value = 21.86, p -value triangular versus square cells = 0.03, p -value triangular versus circular cells = 0.0014, p -value square versus circular cells = 0.048); Fig. 4g adGFP (F -value = 16.36, p -value triangular versus circular cells = 0.004); Fig. 5b (F -value = 14.09, p -value circular versus square cells = 0.002, p -value triangular versus circular cells = 3.15×10^{-4}); Fig. 5e adPI3K (F -value = 14.09, p -value circular versus square cells = 4.82393×10^{-4} , p -value triangular versus circular cells = 2.02886×10^{-4}); Fig. 5e adGFP (F -value = 27.942, p -value circular versus square cells = 0.01094, p -value triangular versus circular cells = 0.0058); Fig. 5g (F -value = 6.13, p -value triangular versus circular cells = 0.0104).

Life Sciences Reporting Summary. Further information on experimental design is available in the Life Sciences Reporting Summary.

Data availability. Raw data is available upon request from rdm-enquiries@imperial.ac.uk.

References

- von Erlach, T. C., Hedegaard, M. A. B. & Stevens, M. M. High resolution Raman spectroscopy mapping of stem cell micropatterns. *Analyst* **140**, 1798–1803 (2015).
- Bertazzo, S., von Erlach, T., Goldoni, S., Çandarlıoğlu, P. L. & Stevens, M. M. Correlative light-ion microscopy for biological applications. *Nanoscale* **4**, 2851–2854 (2012).
- Tan, J. L., Liu, W., Nelson, C. M., Raghavan, S. & Chen, C. S. Simple approach to micropattern cells on common culture substrates by tuning substrate wettability. *Tissue Eng.* **10**, 865–72 (2004).
- Horejs, C. M. et al. Preventing tissue fibrosis by local biomaterials interfacing of specific cryptic extracellular matrix information. *Nat. Commun.* **8**, 1–15 (2017).
- Leight, J. L., Wozniak, M. A., Chen, S., Lynch, M. L. & Chen, C. S. Matrix rigidity regulates a switch between TGF-1-induced apoptosis and epithelial-mesenchymal transition. *Mol. Biol. Cell* **23**, 781–791 (2012).
- Harris, A. R. & Charas, G. T. Experimental validation of atomic force microscopy-based cell elasticity measurements. *Nanotechnology* **22**, 1–10 (2011).
- Herrmann, I. K. et al. Differentiating sepsis from non-infectious systemic inflammation based on microvesicle-bacteria aggregation. *Nanoscale* **7**, 13511–13520 (2015).

Life Sciences Reporting Summary

Nature Research wishes to improve the reproducibility of the work that we publish. This form is intended for publication with all accepted life science papers and provides structure for consistency and transparency in reporting. Every life science submission will use this form; some list items might not apply to an individual manuscript, but all fields must be completed for clarity.

For further information on the points included in this form, see [Reporting Life Sciences Research](#). For further information on Nature Research policies, including our [data availability policy](#), see [Authors & Referees](#) and the [Editorial Policy Checklist](#).

► Experimental design

1. Sample size

Describe how sample size was determined.

Sample size was determined based on prior publication referenced (#2).

2. Data exclusions

Describe any data exclusions.

no data excluded

3. Replication

Describe whether the experimental findings were reliably reproduced.

all replicates were successful

4. Randomization

Describe how samples/organisms/participants were allocated into experimental groups.

not relevant

5. Blinding

Describe whether the investigators were blinded to group allocation during data collection and/or analysis.

FIB microscopy sample analysis and data quantification was performed in a blinded fashion using batch names in order to avoid bias. All other analysis and data acquisition techniques were analyzed non-blinded because of practical reasons and the availability of robust and reproducible measurement and data analysis tools.

Note: all studies involving animals and/or human research participants must disclose whether blinding and randomization were used.

6. Statistical parameters

For all figures and tables that use statistical methods, confirm that the following items are present in relevant figure legends (or in the Methods section if additional space is needed).

- | | |
|--------------------------|--|
| n/a | Confirmed |
| <input type="checkbox"/> | <input checked="" type="checkbox"/> The <u>exact sample size</u> (<i>n</i>) for each experimental group/condition, given as a discrete number and unit of measurement (animals, litters, cultures, etc.) |
| <input type="checkbox"/> | <input checked="" type="checkbox"/> A description of how samples were collected, noting whether measurements were taken from distinct samples or whether the same sample was measured repeatedly |
| <input type="checkbox"/> | <input checked="" type="checkbox"/> A statement indicating how many times each experiment was replicated |
| <input type="checkbox"/> | <input checked="" type="checkbox"/> The statistical test(s) used and whether they are one- or two-sided (note: only common tests should be described solely by name; more complex techniques should be described in the Methods section) |
| <input type="checkbox"/> | <input checked="" type="checkbox"/> A description of any assumptions or corrections, such as an adjustment for multiple comparisons |
| <input type="checkbox"/> | <input checked="" type="checkbox"/> The test results (e.g. <i>P</i> values) given as exact values whenever possible and with confidence intervals noted |
| <input type="checkbox"/> | <input checked="" type="checkbox"/> A clear description of statistics including <u>central tendency</u> (e.g. median, mean) and <u>variation</u> (e.g. standard deviation, interquartile range) |
| <input type="checkbox"/> | <input checked="" type="checkbox"/> Clearly defined error bars |

See the web collection on [statistics for biologists](#) for further resources and guidance.

► Software

Policy information about [availability of computer code](#)

7. Software

Describe the software used to analyze the data in this study.

ImageJ for all image analysis. Matlab for generation of 3D topography maps in Fig. 2. This information is included in the methods section. WHICH SOFTWARE DID YOU USE TO GENERATE PLOTS AND FOR STATISTICAL ANALYSIS?

For manuscripts utilizing custom algorithms or software that are central to the paper but not yet described in the published literature, software must be made available to editors and reviewers upon request. We strongly encourage code deposition in a community repository (e.g. GitHub). *Nature Methods* [guidance for providing algorithms and software for publication](#) provides further information on this topic.

► Materials and reagents

Policy information about [availability of materials](#)

8. Materials availability

Indicate whether there are restrictions on availability of unique materials or if these materials are only available for distribution by a for-profit company.

no restrictions

9. Antibodies

Describe the antibodies used and how they were validated for use in the system under study (i.e. assay and species).

Akt (pan) (11E7) Rabbit mAb #4685: Validated by manufacturer, validated by us (WB)
Phospho-Akt (Thr308) (L32A4) Mouse mAb #5106: Validated by manufacturer, validated by us (WB)
Myosin Light Chain 2 (D18E2) Rabbit mAb #8505: Validated by manufacturer
Phospho-Myosin Light Chain 2 (Ser19) Mouse mAb #3675: Validated by manufacturer
Src (36D10) Rabbit mAb #2109: Validated by manufacturer
PDK1 (D4Q4D) Rabbit mAb #13037: Validated by manufacturer
CD71 (D7S5Z) Rabbit mAb #13208: Validated by manufacturer

10. Eukaryotic cell lines

a. State the source of each eukaryotic cell line used.

human derived mesenchymal stem cells procured from PromoCell

b. Describe the method of cell line authentication used.

cells were authenticated by manufacturer and maintained phenotype over the duration (multiplication number) of our studies (ability to differentiate).

c. Report whether the cell lines were tested for mycoplasma contamination.

Cells were tested and tested negative for mycoplasma contamination

d. If any of the cell lines used are listed in the database of commonly misidentified cell lines maintained by [ICLAC](#), provide a scientific rationale for their use.

no commonly misidentified cell lines used

► Animals and human research participants

Policy information about [studies involving animals](#); when reporting animal research, follow the [ARRIVE guidelines](#)

11. Description of research animals

Provide details on animals and/or animal-derived materials used in the study.

no animals used

Policy information about [studies involving human research participants](#)

12. Description of human research participants

Describe the covariate-relevant population characteristics of the human research participants.

Study did not involve humans